Directing the reactivity of metal hydrides for selective CO_2 reduction

Bianca M. Ceballos[a] and Jenny Y. Yang[a,1]

[a]Department of Chemistry, University of California, Irvine, CA 92697

Edited by Marcetta Y. Darensbourg, Texas A&M University, College Station, TX, and approved October 12, 2018 (received for review July 4, 2018)

A critical challenge in electrocatalytic CO_2 reduction to renewable fuels is product selectivity. Desirable products of CO_2 reduction require proton equivalents, but key catalytic intermediates can also be competent for direct proton reduction to H_2. Understanding how to manage divergent reaction pathways at these shared intermediates is essential to achieving high selectivity. Both proton reduction to hydrogen and CO_2 reduction to formate generally proceed through a metal hydride intermediate. We apply thermodynamic relationships that describe the reactivity of metal hydrides with H^+ and CO_2 to generate a thermodynamic product diagram, which outlines the free energy of product formation as a function of proton activity and hydricity (ΔG_{H-}), or hydride donor strength. The diagram outlines a region of metal hydricity and proton activity in which CO_2 reduction is favorable and H^+ reduction is suppressed. We apply our diagram to inform our selection of $[Pt(dmpe)_2](PF_6)_2$ as a potential catalyst, because the corresponding hydride $[HPt(dmpe)_2]^+$ has the correct hydricity to access the region where selective CO_2 reduction is possible. We validate our choice experimentally; $[Pt(dmpe)_2](PF_6)_2$ is a highly selective electrocatalyst for CO_2 reduction to formate (>90% Faradaic efficiency) at an overpotential of less than 100 mV in acetonitrile with no evidence of catalyst degradation after electrolysis. Our report of a selective catalyst for CO_2 reduction illustrates how our thermodynamic diagrams can guide selective and efficient catalyst discovery.

electrocatalysis | CO_2 reduction | solar fuel | formate production | hydride

The emerging availability of inexpensive renewable electricity has motivated interest in using electrolytic methods to generate sustainable fuels. Electrocatalytic CO_2 reduction provides an entry to carbon-neutral fuels, but product selectivity remains a significant challenge (1, 2). Nearly all reductive reactions of interest involve protons as well as electrons, introducing the complication of direct proton reduction to H_2 under electrolytic conditions. Diversion of electron equivalents into proton reduction results in lower Faradaic efficiency for the desired CO_2 reduction reaction. Various strategies to inhibit or suppress H_2 evolution for heterogeneous (3–7) and homogeneous (8, 9) catalysts have been explored.

To understand the factors that determine selectivity between CO_2 and H^+ reduction, we have been investigating the reactivity of metal hydrides. Selectivity for formate production is particularly challenging because metal hydride intermediates are common to both reaction pathways (Fig. 1). As a result, very few heterogeneous (10–13) or homogeneous (14–16) catalysts have been reported with high (>90%) Faradaic efficiency for formate production. Understanding the reactivity of metal hydrides is key to controlling the bifurcating reaction pathways that ultimately determine selectivity. Most selective catalysts for CO_2 reduction utilize kinetic inhibition (or a high-transition state barrier) to minimize H_2 evolution.

In this report, we utilize a thermodynamic approach to describe the reactivity of metal hydrides with H^+ and CO_2 by applying known free energy relationships (14, 17–28). We depict our findings in a diagram (Fig. 2) that describes the thermodynamic products as a function of hydricity (ΔG_{H-}) (Eq. **1**) of the metal hydride intermediate vs. proton activity (pK_a). Notably, a region is delineated in which select combinations of hydricity and pK_a lead to thermodynamic favorability for selective CO_2 reduction to formate over hydrogen evolution. Since hydricity values have been measured for many classes of compounds and can be predictably tuned through metal and ligand design (29), we believe that the diagrams provide instructive guidelines for targeting the discovery of selective reduction catalysts.

We establish the utility of our diagram by using it to select a known metal hydride $[HPt(dmpe)_2]^+$ with an appropriate hydricity in acetonitrile to access conditions in which selective CO_2 reduction to formate is favorable. We demonstrate that the resting state catalyst $[Pt(dmpe)_2](PF_6)_2$ reduces CO_2 to formate with high Faradaic efficiency and low overpotential.

Results and Discussion

Thermodynamic Product Diagrams. We first describe the construction of the thermodynamic product diagram in acetonitrile (CH_3CN), but the relationships hold in other solvents provided that the correct constants are used (*vide infra*). The thermodynamic cycle describing the free energy for the reaction of a metal hydride toward H^+ to evolve H_2 is shown in Fig. 2. The free energy of H_2 evolution (Eq. **4**) is dependent on the hydricity, pK_a of the acid, and the heterolytic bond forming energy of H_2, which is 77 kcal/mol in acetonitrile (30). Eq. **4** has successfully been applied to identify and optimize electrocatalysts for H_2 evolution (26, 31–38) and H_2 oxidation (31–34, 39–42), and to achieve reversible reactivity (43, 44).

The relationship between pK_a, hydricity, and H_2 evolution in acetonitrile is quantitatively depicted in Fig. 2*A*. The black line

Significance

Electrocatalytic CO_2 reduction to fuels using renewable electricity provides an entry into sustainable carbon-neutral fuels. Most reactions require proton equivalents, but direct proton reduction to H_2 leads to low product selectivity, a significant challenge in the field. The issue of product selectivity arises from shared catalytic intermediates for both CO_2 reduction and H_2 evolution. We describe how thermodynamic relationships regarding the reactivity of H^+ and CO_2 with one of these shared intermediates, homogeneous metal hydrides, can be applied to identify catalyst candidates and conditions where H_2 evolution is suppressed in favor of highly selective CO_2 reduction. The conceptual framework is used to outline operational conditions for electrocatalytic reduction of CO_2 to formate (HCO_2^-) by $[Pt(dmpe)_2](PF_6)_2$ with negligible H_2 production.

Author contributions: B.M.C. and J.Y.Y. designed research; B.M.C. performed research; B.M.C. and J.Y.Y. analyzed data; and J.Y.Y. wrote the paper.

The authors declare no conflict of interest.

This article is a PNAS Direct Submission.

[1]To whom correspondence should be addressed. Email: j.yang@uci.edu.

This article contains supporting information online at www.pnas.org/lookup/suppl/doi:10.1073/pnas.1811396115/-/DCSupplemental.

Published online November 21, 2018.

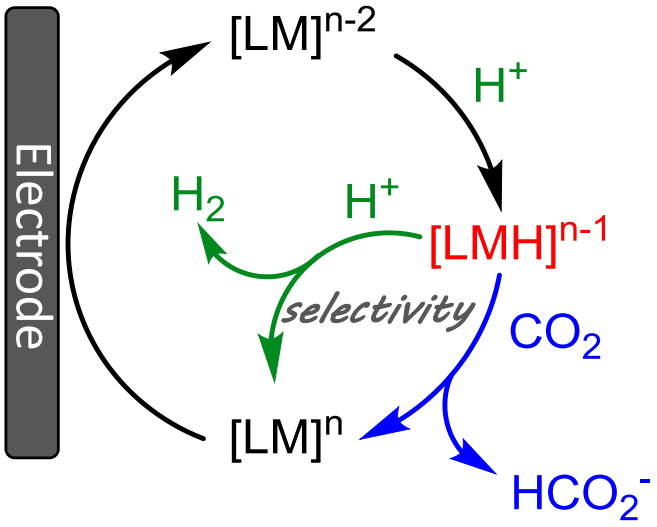

Fig. 1. Proposed catalytic cycles for H^+ and CO_2 reduction.

differentiates the boundary in which the free energy of Eq. **4** in Fig. 2 (ΔG_{H2}) equals zero and $MH/H^+/H_2$ exist in equilibrium, analogous to lines in a Pourbaix diagram. Protonation to evolve hydrogen is exergonic for hydride complexes of a given hydricity under conditions below the black line (green zone) and endergonic above the line (blue zone).

The thermodynamic requirement for reduction of CO_2 to formate, a net hydride transfer, is also dictated by the hydricity (ΔG_{H-}) of the donor as shown in Eq. **6** (Fig. 2). Eq. **6** has been applied to rationalize or predict the activity of the iron-based CO_2 reduction electrocatalyst by Berben and coworkers (20) and CO_2 hydrogenation catalysts (45–50) as well as formate oxidation electrocatalysts (51). Transition metal hydricity values lower than that of formate will result in exergonic hydride transfer to CO_2. This information can be mapped onto the thermodynamic product diagram illustrating metal hydride reactivity with protons (Fig. 2*B*). The thermodynamic product distribution that results from stoichiometric mixtures of metal hydride and acid of specific pK_a values under 1 atm of CO_2 is described in this diagram. The pK_a of formic acid is estimated to be ~20.9 in acetonitrile (52); therefore, it is expected to be protonated at lower pK_a values.

In Fig. 2*B*, a region is defined where specific metal hydricity and pK_a combinations will result in selective reduction of CO_2 to formate without concomitant H_2 evolution (near the bottom right of Fig 2*B*). The challenge of selective CO_2 reduction is often introduced by comparing the thermodynamic potentials for H^+ reduction with CO_2 reduction to formate [−0.028 V (53) vs. −0.150 V (22) vs. $Fe(C_5H_5)_2^{+/0}$ in CH_3CN]. Since the former is more positive than the latter, hydrogen is assumed to be the more favorable thermodynamic product upon reduction. However, these potentials are listed at the standard state (1 M H^+). A full Pourbaix diagram that spans a larger range of proton activity (pK_a) provides a more complete picture (*SI Appendix*, Fig. S1). The thermodynamic potential for proton reduction shifts with the pK_a of the solution by 59 mV per unit according to the Nernst equation for a 2 e^-, 2H^+ process. Similarly, CO_2 reduction to formic acid follows the same relationship until the solution pK_a matches that of formic acid to generate formate. For CO_2 reduction to formate, the thermodynamic potential shifts will deviate in accordance with a 2 e^-, 1H^+ process or 29.5 (59/2) mV per pK_a unit. The smaller decline in thermodynamic potential vs. pK_a compared with H^+ reduction results in a crossing of potentials, where CO_2 reduction to formate occurs at a more positive potential at higher pK_a values and can thus be the more favorable thermodynamic product. The crossing point in the Pourbaix diagram (*SI Appendix*, Fig. S1) matches the pK_a (25.1), which defines the initial point in which selective CO_2 reduction can be achieved in our diagram. A similar crossing in the $2H^+/H_2$ and CO_2/HCO_2^- is observed in Pourbaix diagrams in water (54), although it is complicated by CO_2 equilibria with hydroxide at high pH (55). We believe that our redrawn thermodynamic product diagram, where potential is replaced by hydricity, provides a more instructive guide for targeting catalysts

Heterolytic H_2 Bond Formation

(1) $[LMH]^n \longrightarrow [LM]^{n+1} + H^-$ $\quad \Delta G_{H^-}$

(2) $HB \longrightarrow H^+ + B^-$ $\quad 1.37*pK_a$

(3) $H^+ + H^- \longrightarrow H_2$ $\quad -77$ kcal/mol

(4) $[LMH]^n + HB \longrightarrow [LM]^{n+1} + H_2 + B^-$ $\quad \Delta G_{H2}$

$$\Delta G_{H2} = \Delta G_{H^-} + 1.37*pK_a - 77 \text{ kcal/mol}$$

CO_2 Reduction to HCO_2^-

(1) $[LMH]^n \longrightarrow [LM]^{n+1} + H^-$ $\quad \Delta G_{H^-}$

(5) $CO_2 + H^- \longrightarrow HCO_2^-$ $\quad -\Delta G_{H-}(CO_2)$

(6) $[LMH]^n + CO_2 \longrightarrow [LM]^{n+1} + HCO_2^-$ $\quad \Delta G_{HCO2-}$

$$\Delta G_{HCO2-} = \Delta G_{H^-} - \Delta G_{H-}(CO_2)$$

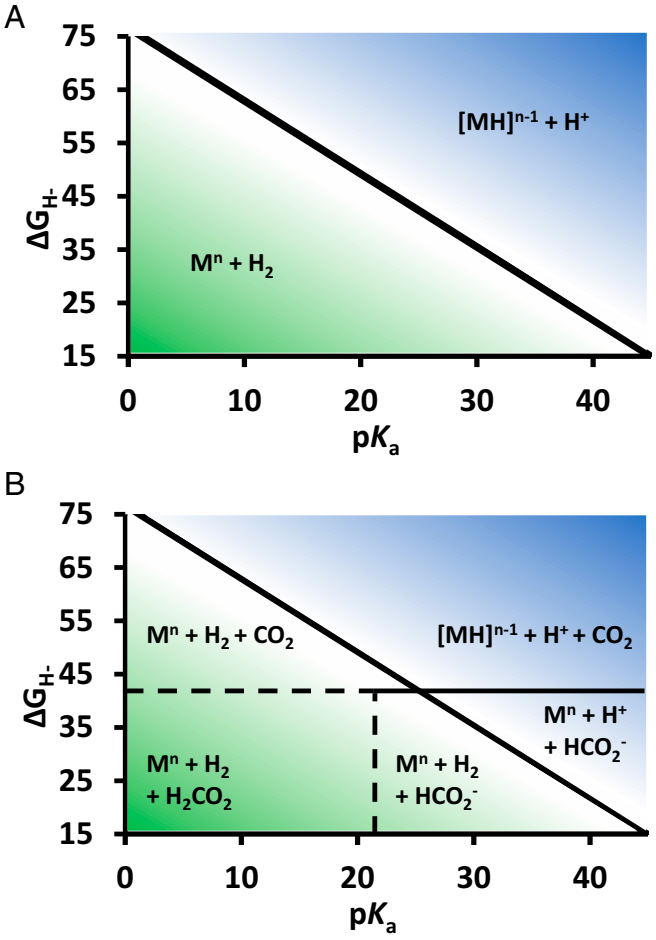

Fig. 2. Free energy calculations for H_2 and HCO_2^- generation from metal hydrides and aqueous thermodynamic product diagrams (*A* and *B*).

to access the region where selective CO_2 reduction is possible, which we demonstrate experimentally herein.

A recently published perspective by Kubiak and coworkers (22) described a primarily linear relationship between hydricity and the one-electron reduction potentials of the parent complex for previously reported groups 8–10 metal hydrides. The perspective provides valuable insight into the relationship between hydricity and reversible redox properties as they pertain to H_2 evolution and CO_2 reduction. However, the authors note that their correlation is qualitative and dependent on similar hydrogen atom transfer bond dissociation free energies among their complexes. Additionally, the authors detail why some metal hydrides deviate significantly from their observed trend and were excluded from the linear fit. We note that the diagrams shown in Fig. 2 are based directly on thermodynamic hydricity values and are thus applicable to all metal hydrides, regardless of metal identity, oxidation state, or ligand environment. The thermodynamic hydricity can also be accurately measured for complexes without reversible redox potentials using methods that have previously been described (19).

Application in other solvents. The diagrams shown in Fig. 2 can be drawn for any solvent provided that the appropriate constants (ΔG_{H2} and ΔG_{HCO2-}) are known in the respective solvent. For example, the diagram illustrating the relationships between metal hydricity and proton activity (similar to Fig. 2*A*) in dimethylsulfoxide (DMSO) is shown in *SI Appendix*, Fig. S2 (ΔG_{H2} = 60.7 kcal/mol in DMSO) (30). The hydricity of formate (ΔG_{HCO2-}) in DMSO is estimated to be 42 kcal/mol (56). The equivalent diagram shown in Fig. 2*B* for DMSO is shown in *SI Appendix*, Fig. S3. We note that we were unable to find a published value for the pK_a of formic acid in DMSO, and therefore, the line between CO_2/HCO_2^- is drawn across the whole range of pK_a values shown. Applying thermodynamic relationships with metal hydricity is most useful in organic solvents with self-consistent data on acid pK_a values. Most measurements of this type have been made in CH_3CN (57–61) and to a lesser extent DMSO (62), but additional values in various solvents are continually being reported.

ΔG_{H2} and ΔG_{HCO2-} have also been reported in aqueous solution (34.2 and 24.1 kcal/mol, respectively) (17). The analogous diagrams in Fig. 2 *A* and *B* are shown in *SI Appendix*, Figs. S4 and S5, respectively. However, the diagrams do not account for the equilibria between CO_2 and OH^- to form HCO_3^- and CO_3^{2-}, which become more significant at higher pH values.

The hydricity value (ΔG_{H-}) for metal hydrides also has a solvent dependence. Multiple studies have measured how solvent affects the hydricity values (14, 18, 19, 23–25, 27, 35). Hydricity values for transition metal hydrides tend to be lower and span a narrower range in solvents with higher dielectric constants, but their absolute values do not change in a predictable fashion by solvent. However, a notable trend is that hydricity values for transition metal hydrides in organic solvents tend to decline to a greater magnitude (become better donors) in water compared to HCO_2^- (ΔG_{HCO2-}). As a result, there are a few examples where CO_2 reduction to HCO_2^- is exergonic in water but endergonic in organic solvents (14, 27, 48). Additionally, detailed studies by Miller and coworkers (63) determined that aqueous hydricity can also be dependent on anions commonly found in aqueous buffers as well as hydroxide at higher pH values.

Kinetic vs. thermodynamic selectivity. The diagrams depicted in this study delineate how to achieve thermodynamic selectivity for CO_2 reduction. In CH_3CN, DMSO, and H_2O, thermodynamic selectivity can only be achieved at modest or low proton activity (pK_a > 25.9 in CH_3CN, pK_a > 13.6 in DMSO, and pH > 8.1 in H_2O). However, kinetic barriers for protonation can be applied to achieve selectivity for CO_2 reduction under more acidic conditions. The difference in kinetic selectivity will still have to compensate for larger free energies of protonation of the metal hydride to form hydrogen at lower pK_a/pH values. Consistent with the free energy associated with H_2 and HCO_2^- formation (Eqs. **4** and **7**, respectively) the only two molecular catalysts with >90% selectivity for formate generation function optimally at modest to high pK_a/pH conditions, with decreasing selectivity at lower proton activities (16, 20). Yet, both maintain fairly high selectivity under more acidic conditions, indicating that the product distribution is also under kinetic control (64).

Application of Thermodynamic Product Diagrams for Catalyst Discovery. To target the region in Fig. 2*B* where selective CO_2 reduction to HCO_2^- in CH_3CN is dictated by the thermodynamic Eqs. **4** and **6**, we selected $[Pt(dmpe)_2](PF_6)_2$ (**3**) as a possible catalyst. The corresponding hydride $[HPt(dmpe)_2](PF_6)$ (**2**) has an experimentally measured hydricity (ΔG_{H-}) (Eq. **1**) of 41.4 kcal/mol (Fig. 2) (19, 65). Consistent with Eq. **6**, $[HPt(dmpe)_2](PF_6)$ reacts stoichiometrically with CO_2 to give HCO_2^- and $[Pt(dmpe)_2](PF_6)_2$ (**3**) (21). The preparation and characterization of the hydride precursor $Pt(dmpe)_2$ (**1**) along with **2** and **3** have been previously reported (65, 66). Complexes **1**, **2**, and **3** are diamagnetic with easily distinguishable $^{31}P\{^1H\}$NMR spectral signatures.

According to Eq. **4** and Fig. 2, the threshold for H_2 evolution with $[HPt(dmpe)_2](PF_6)$ (**2**) is at a pK_a of 25. Acids with pK_a values lower than 25 will be exergonic for H_2 evolution. As expected, stoichiometric reaction of $[HPt(dmpe)_2](PF_6)$ (**2**) with acids, such as anilinium tetrafluoroborate (pK_a = 10.62) and protonated 1,8-diazabicyclo[5.4.0]undec-7-ene (pK_a = 24.34) in CH_3CN (60), results in protonation to give H_2 and $[Pt(dmpe)_2](PF_6)_2$ (**3**) (*SI Appendix*, Figs. S6 and S7). In contrast, $[HPt(dmpe)_2](PF_6)$ (**2**) is stable to protonation using acids with higher pK_a values (ΔG_{H2} > 0), which we demonstrate experimentally. No reaction is observed with $[HPt(dmpe)_2](PF_6)$ (**2**) upon addition of phenol (pK_a = 29.1) (*SI Appendix*, Fig. S8) (62). According to Eq. **4**, H_2 evolution with $[HPt(dmpe)_2](PF_6)$ (**2**) and phenol has an endergonic free energy of 5.5 kcal/mol.

The pK_a (31.1) (65) of the metal hydride provides an upper bound on acids that can be used for metal hydride generation. As a result, $[HPt(dmpe)_2](PF_6)$ (**2**) can be selectively generated at an electrode using proton sources with pK_a values between 31.1 and 25. Therefore, phenol (pK_a = 29.1) is sufficiently acidic to generate $[HPt(dmpe)_2](PF_6)$ (**2**) without additional protonation to evolve H_2.

Selective electrocatalytic reduction of CO_2 to formate. $[Pt(dmpe)_2](PF_6)_2$ (**3**) exhibits a 2 e^- reduction to $[Pt(dmpe)_2]$ (**1**) at −1.73 V vs. $Fe(C_5H_5)_2^{+/0}$ in acetonitrile (Fig. 3, black trace). Electrochemical reduction of **3** to **1** in the presence of phenol results in a loss of reversibility (blue trace in Fig. 3), which we attribute to formation of the hydride **2** [electron transfer (E) followed by a chemical step (C), protonation, or an EC step]. Higher concentrations of phenol do not result in an increase in current (green trace in Fig. 3).

According to Eq. **5**, $[HPt(dmpe)_2](PF_6)$ (**2**) is sufficiently hydritic to react with CO_2 to generate formate ($\Delta G°$ in Eq. **6** = −2.6 kcal/mol). The cyclic voltammogram on addition of 1 atm of CO_2 to **3** with phenol is shown by the red trace in Fig. 3. Titration with increasing concentrations of phenol results in an increase in current (Fig. 3), which is indicative of electrocatalysis. The current reaches a maximum at 10 equivalents.

A proposed catalytic cycle for CO_2 reduction to formate with thermodynamic parameters ($E_{1/2}$ for e^- transfer and pK_a for protonation reactions) for each step is depicted in Fig. 4.

Electrolysis was performed at −2.4 V vs. $Fe(C_5H_5)_2^{+/0}$ under 1 atm of CO_2 (1 mM **3** in 10 mM phenol) for 1 h (*SI Appendix*, Figs. S9 and S10). The concentration of formate in solution after electrolysis was measured using two different methods. The first method used an internal dimethylforamide (DMF) standard to quantify formate by ^1H NMR spectroscopy (*SI Appendix*, Fig. S11). The second method required acidifying the postelectrolysis

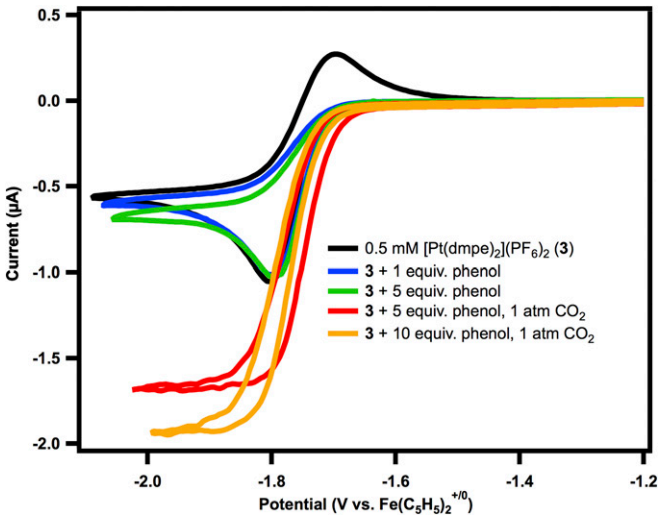

Fig. 3. Cyclic voltammetry under 1 atm of N_2 of 0.5 mM solution of [Pt(dmpe)$_2$](PF$_6$)$_2$ (**3**) (black); after addition of 1 equivalent of phenol (blue); and 5 equivalents of phenol (green); and under 1 atm of CO_2 with 5 equivalents of phenol (red); and 10 equivalents of phenol (orange). Conditions: 0.1 M Et_4NPF_6, 1 mM Fe(C_5H_5)$_2$ present as an internal reference, glassy carbon working and auxiliary electrode, Ag/AgCl pseudoreference electrode, 10 mV/s scan rate.

solution with HCl and quantifying the formic acid with a DMF internal standard using ^{1}H NMR spectroscopy (*SI Appendix*, Fig. S12). The Faradaic efficiency for formate production from either method was greater than 90%. The headspace of the cell was analyzed by GC to detect and quantify H_2 and CO production. A small amount of H_2 (<0.1%) was sometimes observed, but CO was never detected. ^{31}P{^{1}H} NMR spectra of the pre- and postelectrolysis solution display a single resonance that corresponds to **3**. Quantification by integration relative to the PF_6^- anion (*SI Appendix*, Figs. S13 and S14) confirms retention of the catalyst after electrolysis.

The maximum catalytic current observed in the cyclic voltammetry (Fig. 3, orange trace) and the peak current under noncatalytic conditions (Fig. 3, black trace) was used to estimate an observed rate constant (k_{obs}) of 0.5 s^{-1} (*SI Appendix*, Eq. **S4**) (67, 68) for CO_2 reduction to formate. The standard potential for CO_2 reduction to formate in acetonitrile was recently estimated (22). The thermodynamic potential under our conditions (pK_a of 29.1) is E° = −1.64 V. Using the half-wave potential $E°_{1/2}$ = −1.73 V (69), the overpotential for catalysis is 90 mV.

To quantify any potential H_2 or formate generated directly at the electrode, an equivalent electrolysis in the absence of any Pt compound was performed (*SI Appendix*, Fig. S15). Analysis of the headspace by GC detected the presence of <0.1% mL H_2, no CO, and no formate in solution by ^{1}H NMR spectroscopy. Calibration curves for H_2 and formate quantification are shown in *SI Appendix*, Figs. S16 and S17, respectively.

General considerations. The diagrams in Fig. 2 informed our choice of [Pt(dmpe)$_2$](PF$_6$)$_2$ (**3**) as a good catalyst candidate for selective CO_2 reduction to formate. The hydricity of the corresponding hydride [HPt(dmpe)$_2$](PF$_6$) (**2**) is sufficient to reduce CO_2, and there are appropriate acids to access the region of selective reduction. Although the thermodynamic framework described herein proved effective for [Pt(dmpe)$_2$]$^{2+}$ (**3**), some considerations on its application to other potential catalysts are discussed.

Although nearly all molecular hydrogen evolution reaction (HER) catalysts involve a metal hydride intermediate, H–H bond formation can occur through two distinct mechanisms: bimolecular (homolytic) or heterolytic (protonation; as described here). There are cases where both homolytic and heterolytic H_2-forming pathways are viable, such as in the well-studied cobaloxime HER catalysts (70–72), with the predominant operating mechanism dependent on the specific reaction conditions (73–80). The free energy of homolytic H–H bond formation is dependent on the homolytic bond energy of the metal hydride and H_2 and is not expected to have a dependence on the proton activity.

Consequently, the thermodynamic framework described in Fig. 2 is most useful for metal hydrides that are stable to homolytic H_2 bond formation. This is generally true for many classes of transition metal hydrides, including those in the [Ni(P$_2$N$_2$)$_2$]$^{2+}$ class of catalysts (70, 71, 78–91), the water soluble [HNi(DHMPE)$_2$]$^{2+}$, and the subject of these studies [HPt(dmpe)$_2$](PF$_6$)$_2$ (**2**). [The ^{31}P{^{1}H}NMR spectra of [HPt(dmpe)$_2$](PF$_6$)$_2$ (**2**) in acetonitrile show no change over 23 h, confirming that there is no appreciable homolytic pathway for H_2 generation (*SI Appendix*, Fig. S18).] Application of these guidelines to metal hydrides prone to homocoupling to form H_2 would be expected to impact the pH-dependent H_2 evolution activity, present challenges to isolating the metal hydride under electrolytic conditions without generating H_2, and lead to lower overall selectivity.

The reduction potential required to generate [HPt(dmpe)$_2$](PF$_6$) (**2**) from the resting-state catalyst [Pt(dmpe)$_2$](PF$_6$)$_2$ (**3**) (shown as E_{red1} in Eq. **7**) is positive of the reduction potential for **2** (E_{red2} in Eq. **7**):

$$[LM]^{n+1} \xrightarrow[E_{red1}]{2e^-, H^+} [LMH]^n \xrightarrow[E_{red2}]{e^-} [LMH]^{n-1}. \qquad [7]$$

Facile electrolytic generation of [HPt(dmpe)$_2$](PF$_6$) (**2**) is possible, because E_{red1} is greater than E_{red2} (−1.7 vs. −2.8 V vs. Fe(C_5H_5)$_2^{+/0}$) (shown in *SI Appendix*, Fig. S19). As a result, additional reduction of [HPt(dmpe)$_2$](PF$_6$) (**2**) to another intermediate is not possible at the electrochemical potential required to reduce **3**. Several other group 10 metal hydride complexes (26) along with multiple cobalt hydride complexes (84, 88, 92–94) have the same property; reduction of the hydride complex ([LMH]^n in Eq. **7**) is more challenging than reduction of the parent complex ([LM]$^{n+1}$ in Eq. **7**) to generate the hydride (or $E_{red1} > E_{red2}$). In cases where this property does not hold [i.e., the reduction potential of the hydride intermediate (E_{red2}) is positive of the parent complex], it will likely be reduced under electrolytic conditions to generate a stronger hydride donor. For example, cobaloxime hydride

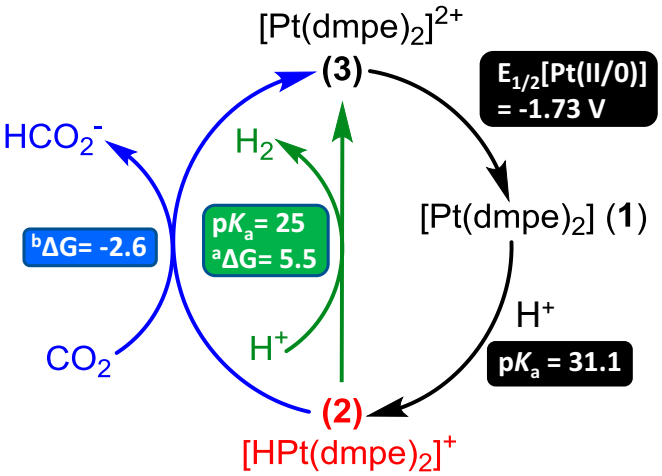

Fig. 4. Proposed catalytic cycle and thermodynamic properties. [a]Free energy for H_2 evolution (kilocalories per mole) calculated from Eq. **4** with an equivalent of phenol. [b]Free energy of hydride transfer (kilocalories per mole) to form formate under 1 atm of CO_2 calculated using Eq. **6**.

complexes will generally be reduced further at potentials necessary to generate the hydride $[LMH]^n$ in Eq. **7** (or $E_{red2} > E_{red1}$). In these cases, the hydricity of the reduced complex ($[LMH]^{n-1}$ in Eq. **7**) can be applied to understand the pK_a-dependent hydrogen evolution catalysis, as $[LMH]^{n-1}$ will likely be generated under electrolytic conditions.

Conclusion

Despite immense interest in electrolytic fuel generation, there are few guidelines for the rational design of catalysts for selective CO_2 reduction. We use thermodynamic relationships to understand the reactivity of metal hydrides, a branch point in the reactivity for formation of either H_2 or HCO_2^-. We applied our analysis to construct a diagram that defines catalyst parameters for achieving selective CO_2 reduction by targeting an appropriate hydricity. Hydricity is akin to an activity descriptor for H_2 and HCO_2^- generation—a thermodynamic quantity that describes the bond energy of a key intermediate. Like an activity descriptor, hydricity is general across many classes of compounds, expanding its utility. Identifying descriptors in molecular systems is particularly advantageous, as bond energies are easily tuned through metal–ligand design.

We applied our thermodynamic product diagram to identify a metal hydride with appropriate hydricity to reduce CO_2 to formate under conditions that minimized concomitant H_2 evolution. We expect that the thermodynamic framework described herein will continue to stimulate the discovery of more selective and efficient catalysts necessary for a carbon-neutral energy economy.

Methods

Experimental details, cyclic voltammograms, NMR spectra, data from electrolysis, H_2 (GC) and HCO_2^- (NMR) calibration curves, and additional thermodynamic product diagrams in DMSO and H_2O are provided in *SI Appendix*. *SI Appendix* includes synthetic methods and materials, physical methods, electrochemical methods (including controlled potential electrolysis and product analysis), additional thermodynamic product diagrams, and NMR spectra.

ACKNOWLEDGMENTS. This material is based on work supported by US Department of Energy, Office of Science, Office of Basic Energy Sciences Award DE-SC0012150. B.M.C. acknowledges support from National Science Foundation Graduate Research Fellowship Grant DGE 1321846. J.Y.Y. acknowledges support as a Sloan Foundation Fellow and a Canadian Institute for Advanced Research (CIFAR) Azrieli Global Scholar in the Bio-Inspired Solar Energy Program.

1. Seh ZW, et al. (2017) Combining theory and experiment in electrocatalysis: Insights into materials design. *Science* 355:eaad4998.
2. Inglis JL, MacLean BJ, Pryce MT, Vos JG (2012) Electrocatalytic pathways towards sustainable fuel production from water and CO2. *Coord Chem Rev* 256:2571–2600.
3. Li CW, Ciston J, Kanan MW (2014) Electroreduction of carbon monoxide to liquid fuel on oxide-derived nanocrystalline copper. *Nature* 508:504–507.
4. Mariano RG, McKelvey K, White HS, Kanan MW (2017) Selective increase in CO_2 electroreduction activity at grain-boundary surface terminations. *Science* 358: 1187–1192.
5. Wang Y, Liu J, Wang Y, Al-Enizi AM, Zheng G (2017) Tuning of CO_2 reduction selectivity on metal electrocatalysts. *Small* 13:1701809.
6. Feaster JT, et al. (2017) Understanding selectivity for the electrochemical reduction of carbon dioxide to formic acid and carbon monoxide on metal electrodes. *ACS Catal* 7: 4822–4827.
7. Cave ER, et al. (2018) Trends in the catalytic activity of hydrogen evolution during CO2 electroreduction on transition metals. *ACS Catal* 8:3035–3040.
8. Elgrishi N, Chambers MB, Fontecave M (2015) Turning it off! Disfavouring hydrogen evolution to enhance selectivity for CO production during homogeneous CO_2 reduction by cobalt-terpyridine complexes. *Chem Sci (Camb)* 6:2522–2531.
9. Fogeron T, et al. (2018) A bioinspired nickel(bis-dithiolene) complex as a homogeneous catalyst for carbon dioxide electroreduction. *ACS Catal* 8:2030–2038.
10. Podlovchenko BI, Kolyadko EA, Lu S (1994) Electroreduction of carbon dioxide on palladium electrodes at potentials higher than the reversible hydrogen potential. *J Electroanal Chem* 373:185–187.
11. Min X, Kanan MW (2015) Pd-catalyzed electrohydrogenation of carbon dioxide to formate: High mass activity at low overpotential and identification of the deactivation pathway. *J Am Chem Soc* 137:4701–4708.
12. Lee CH, Kanan MW (2015) Controlling H+ vs CO2 reduction selectivity on Pb electrodes. *ACS Catal* 5:465–469.
13. Zhang S, Kang P, Meyer TJ (2014) Nanostructured tin catalysts for selective electrochemical reduction of carbon dioxide to formate. *J Am Chem Soc* 136:1734–1737.
14. Taheri A, Thompson EJ, Fettinger JC, Berben LA (2015) An iron electrocatalyst for selective reduction of CO2 to formate in water: Including thermochemical insights. *ACS Catal* 5:7140–7151.
15. Roy S, et al. (2017) Molecular cobalt complexes with pendant amines for selective electrocatalytic reduction of carbon dioxide to formic acid. *J Am Chem Soc* 139: 3685–3696.
16. Kang P, et al. (2012) Selective electrocatalytic reduction of CO2 to formate by water-stable iridium dihydride pincer complexes. *J Am Chem Soc* 134:5500–5503.
17. Connelly SJ, Wiedner ES, Appel AM (2015) Predicting the reactivity of hydride donors in water: Thermodynamic constants for hydrogen. *Dalton Trans* 44:5933–5938.
18. Muckerman JT, Achord P, Creutz C, Polyansky DE, Fujita E (2012) Calculation of thermodynamic hydricities and the design of hydride donors for CO2 reduction. *Proc Natl Acad Sci USA* 109:15657–15662.
19. Wiedner ES, et al. (2016) Thermodynamic hydricity of transition metal hydrides. *Chem Rev* 116:8655–8692.
20. Loewen ND, Neelakantan TV, Berben LA (2017) Renewable formate from C-H bond formation with CO_2: Using iron carbonyl clusters as electrocatalysts. *Acc Chem Res* 50: 2362–2370.
21. DuBois DL, Berning DE (2000) Hydricity of transition-metal hydrides and its role in CO2 reduction. *Appl Organomet Chem* 14:860–862.
22. Waldie KM, Ostericher AL, Reineke MH, Sasayama AF, Kubiak CP (2018) Hydricity of transition-metal hydrides: Thermodynamic considerations for CO2 reduction. *ACS Catal* 8:1313–1324.
23. Matsubara Y, Fujita E, Doherty MD, Muckerman JT, Creutz C (2012) Thermodynamic and kinetic hydricity of ruthenium(II) hydride complexes. *J Am Chem Soc* 134: 15743–15757.
24. Creutz C, Chou MH (2007) Rapid transfer of hydride ion from a ruthenium complex to C1 species in water. *J Am Chem Soc* 129:10108–10109.
25. Tsay C, Livesay BN, Ruelas S, Yang JY (2015) Solvation effects on transition metal hydricity. *J Am Chem Soc* 137:14114–14121.
26. Tsay C, Yang JY (2016) Electrocatalytic hydrogen evolution under acidic aqueous conditions and mechanistic studies of a highly stable molecular catalyst. *J Am Chem Soc* 138:14174–14177.
27. Ceballos BM, Tsay C, Yang JY (2017) CO_2 reduction or HCO_2^- oxidation? Solvent-dependent thermochemistry of a nickel hydride complex. *Chem Commun (Camb)* 53:7405–7408.
28. Taheri A, Berben LA (2016) Tailoring electrocatalysts for selective CO2 or H(+) reduction: Iron carbonyl clusters as a case study. *Inorg Chem* 55:378–385.
29. Brereton KR, et al. (2016) Aqueous hydricity from calculations of reduction potential and acidity in water. *J Phys Chem B* 120:12911–12919.
30. Wayner DDM, Parker VD (1993) Bond energies in solution from electrode potentials and thermochemical cycles. A simplified and general approach. *Acc Chem Res* 26: 287–294.
31. Wilson AD, et al. (2006) Hydrogen oxidation and production using nickel-based molecular catalysts with positioned proton relays. *J Am Chem Soc* 128:358–366.
32. Fraze K, Wilson AD, Appel AM, Rakowski DuBois M, DuBois DL (2007) Thermodynamic properties of the Ni–H bond in complexes of the type [HNi(P2RN2R′)2](BF4) and evaluation of factors that control catalytic activity for hydrogen oxidation/production. *Organometallics* 26:3918–3924.
33. Rakowski DuBois M, DuBois DL (2009) Development of molecular electrocatalysts for CO2 reduction and H2 production/oxidation. *Acc Chem Res* 42:1974–1982.
34. Yang JY, Bullock RM, DuBois MR, DuBois DL (2011) Fast and efficient molecular electrocatalysts for H2 production: Using hydrogenase enzymes as guides. *MRS Bull* 36:39–47.
35. Brereton KR, Pitman CL, Cundari TR, Miller AJM (2016) Solvent-dependent thermochemistry of an iridium/ruthenium H_2 evolution catalyst. *Inorg Chem* 55:12042–12051.
36. Wiese S, Kilgore UJ, DuBois DL, Bullock RM (2012) [Ni(PMe2NPh2)2](BF4)2 as an electrocatalyst for H2 production. *ACS Catal* 2:720–727.
37. Kilgore UJ, et al. (2011) Studies of a series of [Ni(P(R)2N(Ph)2)2(CH3CN)]2+ complexes as electrocatalysts for H2 production: Substituent variation at the phosphorus atom of the P2N2 ligand. *Inorg Chem* 50:10908–10918.
38. Tsay C, Ceballos BM, Yang JY (October 8, 2018) pH-dependent reactivity of a water-soluble nickel complex: Hydrogen evolution vs selective electrochemical hydride generation. *Organometallics*, 10.1021/acs.organomet.8b00558.
39. Curtis CJ, et al. (2003) [Ni(Et2PCH2NMeCH2PEt2)2]2+ as a functional model for hydrogenases. *Inorg Chem* 42:216–227.
40. Yang JY, et al. (2010) Hydrogen oxidation catalysis by a nickel diphosphine complex with pendant tert-butyl amines. *Chem Commun (Camb)* 46:8618–8620.
41. Liu T, Dubois DL, Bullock RM (2013) An iron complex with pendent amines as a molecular electrocatalyst for oxidation of hydrogen. *Nat Chem* 5:228–233.
42. Liu T, et al. (2015) Iron complexes bearing diphosphine ligands with positioned pendant amines as electrocatalysts for the oxidation of H2. *Organometallics* 34: 2747–2764.
43. Smith SE, Yang JY, DuBois DL, Bullock RM (2012) Reversible electrocatalytic production and oxidation of hydrogen at low overpotentials by a functional hydrogenase mimic. *Angew Chem Int Ed Engl* 51:3152–3155.

44. Priyadarshani N, et al. (2016) Achieving reversible H2/H+ interconversion at room temperature with enzyme-inspired molecular complexes: A mechanistic study. *ACS Catal* 6:6037–6049.
45. Jeletic MS, Mock MT, Appel AM, Linehan JC (2013) A cobalt-based catalyst for the hydrogenation of CO2 under ambient conditions. *J Am Chem Soc* 135:11533–11536.
46. Zall CM, Linehan JC, Appel AM (2015) A molecular copper catalyst for hydrogenation of CO2 to formate. *ACS Catal* 5:5301–5305.
47. Cammarota RC, et al. (2017) A bimetallic nickel-gallium complex catalyzes CO_2 hydrogenation via the intermediacy of an anionic d^{10} nickel hydride. *J Am Chem Soc* 139:14244–14250.
48. Burgess SA, Appel AM, Linehan JC, Wiedner ES (2017) Changing the mechanism for CO_2 hydrogenation using solvent-dependent thermodynamics. *Angew Chem Int Ed Engl* 56:15002–15005.
49. Burgess SA, Kendall AJ, Tyler DR, Linehan JC, Appel AM (2017) Hydrogenation of CO2 in water using a bis(diphosphine) Ni–H complex. *ACS Catal* 7:3089–3096.
50. Lilio AM, et al. (2015) Incorporation of pendant bases into Rh(diphosphine)2 complexes: Synthesis, thermodynamic studies, and catalytic CO2 hydrogenation activity of [Rh(P2N2)2](+) complexes. *J Am Chem Soc* 137:8251–8260.
51. Galan BR, et al. (2011) Electrocatalytic oxidation of formate by [Ni(P(R)2N(R′)2)2(CH3CN)]2+ complexes. *J Am Chem Soc* 133:12767–12779.
52. Stirling MJ, Sweeney G, MacRory K, Blacker AJ, Page MI (2016) The kinetics and mechanism of the organo-iridium-catalysed enantioselective reduction of imines. *Org Biomol Chem* 14:3614–3622.
53. Roberts JAS, Bullock RM (2013) Direct determination of equilibrium potentials for hydrogen oxidation/production by open circuit potential measurements in acetonitrile. *Inorg Chem* 52:3823–3835.
54. Costentin C, Robert M, Savéant J-M (2015) Current issues in molecular catalysis illustrated by iron porphyrins as catalysts of the CO2-to-CO electrochemical conversion. *Acc Chem Res* 48:2996–3006.
55. Keene FR (1993) Thermodynamic, kinetic, and product considerations in carbon dioxide reactivity. *Electrochemical and Electrocatalytic Reactions of Carbon Dioxide*, ed Sullivan BP (Elsevier, Amsterdam), pp 1–18.
56. Moret S, Dyson PJ, Laurenczy G (2014) Direct synthesis of formic acid from carbon dioxide by hydrogenation in acidic media. *Nat Commun* 5:4017.
57. Kütt A, et al. (2006) A comprehensive self-consistent spectrophotometric acidity scale of neutral Brønsted acids in acetonitrile. *J Org Chem* 71:2829–2838.
58. Eckert F, et al. (2009) Prediction of acidity in acetonitrile solution with COSMO-RS. *J Comput Chem* 30:799–810.
59. Izutsu K; International Union of Pure and Applied Chemistry. Commission on Electroanalytical Chemistry (1990) *Acid-Base Dissociation Constants in Dipolar Aprotic Solvents* (Blackwell Scientific Publications, Hoboken, NJ).
60. Kaljurand I, et al. (2005) Extension of the self-consistent spectrophotometric basicity scale in acetonitrile to a full span of 28 pKa units: Unification of different basicity scales. *J Org Chem* 70:1019–1028.
61. Lõkov M, et al. (2017) On the basicity of conjugated nitrogen heterocycles in different media. *Eur J Org Chem* 2017:4475–4489.
62. Kütt A, et al. (2008) Pentakis(trifluoromethyl)phenyl, a sterically crowded and electron-withdrawing group: Synthesis and acidity of pentakis(trifluoromethyl)benzene, -toluene, -phenol, and -aniline. *J Org Chem* 73:2607–2620.
63. Pitman CL, Brereton KR, Miller AJM (2016) Aqueous hydricity of late metal catalysts as a continuum tuned by ligands and the medium. *J Am Chem Soc* 138:2252–2260.
64. Johnson SI, Nielsen RJ, Goddard WA (2016) Selectivity for HCO2– over H2 in the electrochemical catalytic reduction of CO2 by (POCOP)IrH2. *ACS Catal* 6:6362–6371.
65. Curtis CJ, Miedaner A, Ellis WW, DuBois DL (2002) Measurement of the hydride donor abilities of [HM(diphosphine)2]+ complexes (M = Ni, Pt) by heterolytic activation of hydrogen. *J Am Chem Soc* 124:1918–1925.
66. Berning DE, Noll BC, DuBois DL (1999) Relative hydride, proton, and hydrogen atom transfer abilities of [HM(diphosphine)2]PF6 complexes (M = Pt, Ni). *J Am Chem Soc* 121:11432–11447.
67. Nicholson RS, Shain I (1964) Theory of stationary electrode polarography. Single scan and cyclic methods applied to reversible, irreversible, and kinetic systems. *Anal Chem* 36:706–723.
68. Saveant JM, Vianello E (1965) Potential-sweep chronoamperometry: Kinetic currents for first-order chemical reaction parallel to electron-transfer process (catalytic currents). *Electrochim Acta* 10:905–920.
69. Appel AM, Helm ML (2014) Determining the overpotential for a molecular electrocatalyst. *ACS Catal* 4:630–633.
70. Muckerman JT, Fujita E (2011) Theoretical studies of the mechanism of catalytic hydrogen production by a cobaloxime. *Chem Commun (Camb)* 47:12456–12458.
71. Solis BH, Hammes-Schiffer S (2011) Theoretical analysis of mechanistic pathways for hydrogen evolution catalyzed by cobaloximes. *Inorg Chem* 50:11252–11262.
72. Dempsey JL, Winkler JR, Gray HB (2010) Kinetics of electron transfer reactions of H2-evolving cobalt diglyoxime catalysts. *J Am Chem Soc* 132:1060–1065.
73. Thoi VS, Sun Y, Long JR, Chang CJ (2013) Complexes of earth-abundant metals for catalytic electrochemical hydrogen generation under aqueous conditions. *Chem Soc Rev* 42:2388–2400.
74. Zee DZ, Chantarojsiri T, Long JR, Chang CJ (2015) Metal-polypyridyl catalysts for electro- and photochemical reduction of water to hydrogen. *Acc Chem Res* 48:2027–2036.
75. Kandemir B, Kubie L, Guo Y, Sheldon B, Bren KL (2016) Hydrogen evolution from water under aerobic conditions catalyzed by a cobalt ATCUN metallopeptide. *Inorg Chem* 55:1355–1357.
76. Eckenhoff WT, Brennessel WW, Eisenberg R (2014) Light-driven hydrogen production from aqueous protons using molybdenum catalysts. *Inorg Chem* 53:9860–9869.
77. Beyene BB, Mane SB, Hung C-H (2015) Highly efficient electrocatalytic hydrogen evolution from neutral aqueous solution by a water-soluble anionic cobalt(II) porphyrin. *Chem Commun (Camb)* 51:15067–15070.
78. Mondal B, et al. (2013) Cobalt corrole catalyst for efficient hydrogen evolution reaction from H2O under ambient conditions: Reactivity, spectroscopy, and density functional theory calculations. *Inorg Chem* 52:3381–3387.
79. McKone JR, Marinescu SC, Brunschwig BS, Winkler JR, Gray HB (2014) Earth-abundant hydrogen evolution electrocatalysts. *Chem Sci (Camb)* 5:865–878.
80. Costentin C, Dridi H, Savéant J-M (2014) Molecular catalysis of H2 evolution: Diagnosing heterolytic versus homolytic pathways. *J Am Chem Soc* 136:13727–13734.
81. Wiedner ES, Brown HJS, Helm ML (2016) Kinetic analysis of competitive electrocatalytic pathways: New insights into hydrogen production with nickel electrocatalysts. *J Am Chem Soc* 138:604–616.
82. Elgrishi N, McCarthy BD, Rountree ES, Dempsey JL (2016) Reaction pathways of hydrogen-evolving electrocatalysts: Electrochemical and spectroscopic studies of proton-coupled electron transfer processes. *ACS Catal* 6:3644–3659.
83. Roubelakis MM, Bediako DK, Dogutan DK, Nocera DG (2012) Proton-coupled electron transfer kinetics for the hydrogen evolution reaction of hangman porphyrins. *Energy Environ Sci* 5:7737–7740.
84. Solis BH, et al. (2014) Theoretical analysis of cobalt hangman porphyrins: Ligand dearomatization and mechanistic implications for hydrogen evolution. *ACS Catal* 4:4516–4526.
85. Bediako DK, et al. (2014) Role of pendant proton relays and proton-coupled electron transfer on the hydrogen evolution reaction by nickel hangman porphyrins. *Proc Natl Acad Sci USA* 111:15001–15006.
86. Bhattacharjee A, et al. (2013) A computational study of the mechanism of hydrogen evolution by cobalt(diimine-dioxime) catalysts. *Chemistry* 19:15166–15174.
87. Lee CH, Dogutan DK, Nocera DG (2011) Hydrogen generation by hangman metalloporphyrins. *J Am Chem Soc* 133:8775–8777.
88. Marinescu SC, Winkler JR, Gray HB (2012) Molecular mechanisms of cobalt-catalyzed hydrogen evolution. *Proc Natl Acad Sci USA* 109:15127–15131.
89. Solis BH, Hammes-Schiffer S (2011) Substituent effects on cobalt diglyoxime catalysts for hydrogen evolution. *J Am Chem Soc* 133:19036–19039.
90. Razavet M, Artero V, Fontecave M (2005) Proton electroreduction catalyzed by cobaloximes: Functional models for hydrogenases. *Inorg Chem* 44:4786–4795.
91. Baffert C, Artero V, Fontecave M (2007) Cobaloximes as functional models for hydrogenases. 2. Proton electroreduction catalyzed by difluoroborylbis(dimethylglyoximato)cobalt(II) complexes in organic media. *Inorg Chem* 46:1817–1824.
92. Fang M, et al. (2014) Cobalt complexes containing pendant amines in the second coordination sphere as electrocatalysts for H2 production. *Organometallics* 33:5820–5833.
93. Koelle U, Paul S (1986) Electrochemical reduction of protonated cyclopentadienylcobalt phosphine complexes. *Inorg Chem* 25:2689–2694.
94. Wiedner ES, Bullock RM (2016) Electrochemical detection of transient cobalt hydride intermediates of electrocatalytic hydrogen production. *J Am Chem Soc* 138:8309–8318.